# Phosphorous incorporation in $Pd_2Sn$ alloys for electrocatalytic ethanol oxidation

Xiaoting Yu [a,b], Junfeng Liu[c,*], Junshan Li [a,b], Zhishan Luo [d,e], Yong Zuo[a,b], Congcong Xing [a,f], Jordi Llorca[f], Jordi Arbiol [g,h], Kai Pan[i], Ying Xie[i,*], Andreu Cabot [a,h,*]

a Catalonia Institute for Energy Research - IREC, Sant Adrià de Besòs, 08930 Barcelona, Spain

b Department of Electronic and Biomedical Engineering, Universitat de Barcelona, 08028 Barcelona, Spain

c Institute for Energy Research, School of Chemistry and Chemical Engineering, Jiangsu University, 212013 Zhenjiang, P.R. China

d Department of Chemistry, Southern University of Science and Technology (SUSTech),518055 Shenzhen, Guangdong, P. R. China

e SUSTech Academy for Advanced Interdisciplinary Studies, Southern University of Science and Technology (SUSTech), 518055 Shenzhen, Guangdong, P. R. China

f Institute of Energy Technologies, Department of Chemical Engineering and Barcelona Research Center in Multiscale Science and Engineering, Universitat Politècnica de Catalunya, EEBE, 08019 Barcelona, Spain

g Catalan Institute of Nanoscience and Nanotechnology (ICN2), CSIC and BIST, Campus UAB, Bellaterra, 08193 Barcelona, Spain

h ICREA, Pg. Lluís Companys 23, 08010 Barcelona, Spain

i Key Laboratory of Functional Inorganic Material Chemistry, Ministry of Education, Heilongjiang University, 150080 Harbin, P.R. China

**ABSTRACT**

Direct ethanol fuel cells (DEFCs) offer multiple advantages to power electric vehicles and portable electronics, but their deployment is currently limited by the unavailability of proper electrocatalysis for the ethanol oxidation reaction (EOR). In this work, we optimize the performance of Pd-based electrocatalysts by alloying Pd with Sn and P. We first detail a synthetic method to produce $Pd_2SnP_x$ nanorods that incorporate up to 40 % of phosphorus. These nanorods are supported on carbon black and tested for EOR. $Pd_2SnP_x$/C catalysts exhibit mass current densities up to 4.89 A $mg_{Pd}^{-1}$, well above those of $Pd_2Sn$/C, $PdP_2$/C and Pd/C reference catalysts. Furthermore, a twofold lower Tafel slope and a much longer durability are demonstrated for the $Pd_2SnP_x$/C catalyst. The performance improvement is rationalized with the aid of DFT calculations and is associated with a combination of an electronic and a bifunctional effect.

## 1. INTRODUCTION

Direct liquid fuel cells provide a means for the straight conversion of chemical energy within a liquid fuel into electricity. As liquid fuel, ethanol offers a large energy density (8.01 KW h $kg^{-1}$), low toxicity, relatively high boiling point for safe storage, transportation and operation, and potential for bio-sourcing.[1,2] These advantages make direct ethanol fuel cells (DEFCs) extremely appealing to power electric vehicles and portable electronics, among other. However, the deployment of DEFCs is being hampered by the high cost and moderate performances of current electrocatalysts for the ethanol oxidation reaction (EOR).[3]

Pt and Pt-based alloys have been the most studied and optimized EOR catalysts to date, particularly in acidic conditions, but their high cost limits their application.[4] Compared with acid electrolytes, alkaline solutions are less corrosive and provide faster reaction kinetics for both alcohol oxidation and oxygen reduction, which enable the use of a larger variety of catalysts.[5] These advantages together with the recent development of high-performance anion exchange membranes, have moved interest from acid- to basic-type DEFCs and from Pt to less costly catalysts. Moving away from Pt-based catalysts in alkaline solution, increasing attention is being paid to Pd, which offers lower cost, better resistance to poisoning and similar or even better catalytic activities.[6-8] We and others have recently demonstrated that alloying Pd with Sn and optimizing the catalyst crystallographic facets significantly improve EOR performances through a combination of electronic and bifunctional effects.[9-12] We have also recently reported that the incorporation of phosphorous into Pd catalyst strongly improves its EOR performance by other mechanisms.[13] Phosphorous inclusion provides advantages in terms of introducing additional adsorption sites,[14,15] slightly modifying the electronic structure of Pd,[16] shifting the Pd oxide formation to higher potentials that in turn results in a better stability,[17] and potentially reducing the amount of Pd required to reach a certain catalytic activity, thus further reducing the overall catalyst cost.[15,18-24]

Herein we report an approach to prepare Pd nanocrystals that incorporate both elements, Sn and P. We produced $Pd_2SnP_x$ by reacting intermetallic $Pd_2Sn$ with a phosphorous precursor during the nanoparticle growth stage. As-synthesized nanoparticles were supported on carbon black and tested toward ethanol oxidation in alkaline media. DFT calculations were used to identify the relationship between the measured performances and the catalyst composition.

## 2. EXPERIMENTAL

### *2.1. Chemicals*

Oleylamine (OAm, 80–90%) was purchased from ACROS Organics. 1-Octadecene (ODE, 90%), palladium(II) acetylacetonate ($Pd(acac)_2$, Pd 34.7wt%), tin(II) acetate ($Sn(OAc)_2$, 99%), hexamethylphosphorous triamide (HMPT, 97%), trioctylphosphine (TOP, 97%), methylamine hydrochloride (MAC, 98%), potassium hydroxide (KOH, 85%), and Nafion (5 wt% in a mixture of low aliphatic alcohols and water) were obtained from Sigma-Aldrich. A reference Pd catalyst, 20% Pd on activated carbon powder, was purchased from Alfa Aesar. Carbon black Vulcan XC-72 was obtained from Fuel Cell Earth. Hexane, ethanol and acetone were of analytical grade and obtained from various sources. MilliQ water was obtained from a PURELAB flex from ELGA. All chemicals were used as received, without further purification.

*2.2. Synthesis of $Pd_2SnP_x$ nanorods*

91.4 mg (0.3 mmol) of $Pd(acac)_2$, 35.5 mg (0.3 mmol) of $Sn(OAc)_2$ and 68.0 mg (1 mmol) of MAC were mixed with 20 mL of OAm in a 50 mL three-neck flask connected to the Schlenk line coupled to an exhaust gas absorption solution (1 M $CuSO_4$). After keeping the precursor mixture under argon flow for 15 min, 1 mL of TOP was introduced. Subsequently, the solution was heated to 100 °C and maintained at this temperature for 1 h. Then temperature was slowly increased to 200 °C at a rate of 5 °C/min and maintained for 30 min. Next, temperature was increased to 300 °C in 40 min. During this temperature increase, the solution turned black indicating the occurrence of the Pd-Sn nanocrystal nucleation.[25] When the solution reached 300 °C, 0.2 mL (1.1 mmol) of HMPT dissolved in 0.5 mL of ODE was injected and the mixture was allowed to react for 1 h before cooling down to ambient temperature. The reaction product was precipitated by adding excess amount of acetone and centrifugation at 5000 rpm for 5 min. Then, it was re-dispersed and re-precipitated 3 times with chloroform and acetone. The final black product was dispersed in hexane.

*2.3. Synthesis of reference nanocrystals: $Pd_2Sn$ and $PdP_2$*

$Pd_2Sn$ nanorods were produced following the exact same protocol described above but without adding HMPT at 300 °C.[25] $PdP_2$ nanocrystals were obtained through the same procedure but without adding $Sn(OAc)_2$ to the initial precursor solution.[13] Nanoparticles were purified as detailed above and the final black precipitates were dispersed in hexane.

*2.4 Catalysts preparation*

$Pd_2SnP_x$/C, $Pd_2Sn$/C and $Pd_2P$/C electrocatalysts were prepared by supporting the corresponding nanocrystals on carbon black.[26] Briefly, 5 mg of $Pd_2SnP_x$ (or $Pd_2Sn$/$Pd_2P$) dispersed in 5 mL of hexane were mixed with 5 mg of Vulcan XC-72 carbon dispersed in

ethanol. The mixture was sonicated for 1 h to homogeneous distribute the nanocrystals over the carbon surface. The product was collected by centrifugation and then dispersed in a mixture of 10 mL ethanol and 1 mL acetic acid to remove surface organic ligands through sonication. After washing with ethanol, the catalyst was dried naturally under ambient condition and then it was annealed at 250 °C in Ar atmosphere for 1h. The final product was dispersed in isopropanol containing 5% Nafion to obtain an ink containing a nanocrystal concentration of 1 mg/mL.

*2.5 Electrochemical measurements.*

Electrochemical measurements were conducted at room temperature with a BioLogic electrochemical workstation using a three-neck-type cell including a Pt gauze as counter electrode and a Hg/HgO (1 M KOH) electrode as reference. The working electrode was prepared by drop-casting 3 μL of the catalyst ink on a 5 mm diameter glassy carbon (GC) electrode and letting it dry naturally. The same mass of particles (or Pd for the commercial sample) was used to prepare each electrode, which translated into lower amounts of Pd on the $Pd_2SnP_x$/C catalyst when compared with the 3 reference catalysts tested. Cyclic voltammetry (CV) curves were recorded at a scan rate of 50 mV $s^{-1}$ in Ar-saturated aqueous solutions that contained 0.5 M KOH or 0.5 M KOH + 0.5 M ethanol. Chronoameperometry (CA) measurements were conducted at -0.1 V vs. Hg/HgO for 7000 s in a 0.5 M KOH + 0.5 M ethanol electrolyte.

*2.6 Structural and chemical characterization*

Powder X-ray diffraction (XRD) patterns were collected from the samples supported on a Si substrate on a Bruker-AXS D8 Advanced X-ray diffractometer with Ni-filtered (2 μm thickness) Cu K radiation (λ=1.5406 Å) operating at 40 kV and 40 mA. Scanning electron microscopy (SEM) analysis was conducted with a ZEISS Auriga microscope equipped with an energy dispersive X-ray spectroscopy (EDS) detector operating at 20 kV. Transmission electron microscopy (TEM) images were carried out with a ZEISS LIBRA 120 operating at 120 kV and a JEOL 1011 at 100 kV. High-resolution TEM (HRTEM) analysis was carried out using a field emission gun FEI™ Tecnai F20 microscope at 200 kV with a point-to-point resolution of 0.19 nm. Annular dark-field scanning transmission electron microscope (HAADF-STEM) was combined with electron energy loss spectroscopy (EELS) in the Tecnai F20 with a GATAN QUANTUM filter. X-ray photoelectron spectroscopy (XPS) was analyzed on a SPECS system equipped with an Al anode XR50 source operating at 150 mW and a Phoibos 150 MCD-9 detector. The pressure of the analysis chamber was below $10^{-7}$ Pa. The CasaXPS program (Casa Software Ltd., UK) was employed for

the data process. Fourier transform infrared spectroscopy (FTIR) was performed on an Alpha Bruker FTIR spectrometer with a platinum attenuated total reflectance (ATR) single reflection module. Thermogravimetric analyses (TGA) were carried out using a PerkinElmer Diamond TG/DTA instrument. Samples were measured in $N_2$ from ambient temperature to 700°C at a heating rate of 5 °C/min.

*2.7 Computational details*

All calculations were performed using the Vienna Ab initio Simulation Package (VASP)[27-30]within the density functional theory (DFT) framework. Perdew-Burke-Ernzerhof (PBE) functional[31] was used to treat the exchange-correlation energy. The projector augmented-wave (PAW)[32] was applied and the energy cutoff was 400 eV. The sampling over Brillouin zone was treated by the Monkhorst-Pack technique,[33] and a (2×2×1) grid was introduced. Geometry optimization process was repeated until the energy change of two adjacent ionic steps is less than $10^{-5}$ eV and the force on the atoms less than -0.03 eV/Å. Furthermore, dispersion interactions were treated on the DFT-D3 level.[34,35] During the calculation, the (2×2×1) supercells for $Pd_2Sn$ (001) and P-modified surfaces were used and displayed in Figure S1. A vacuum slab of 15 Å was applied to avoid the pseudo interactions between the periodic images along z axis. The adsorption energies for $OH^-$ on different sites of the surfaces were calculated based on the following equation,

$$E_{ad.} = E_{OH/slab} - E_{OH^-} - E_{slab} \qquad (1)$$

where $E_{OH/slab}$, $E_{OH-}$, and $E_{slab}$ are the total energies for OH/slab, $OH^-$, and the pure surface, respectively. Furthermore, the energy of $OH^-$ was calculated by, [36]

$$E(\mathrm{OH^-}) = E(\mathrm{H_2O}) - [\tfrac{1}{2}E(\mathrm{H_2}) - PH \times k_B T ln10] \qquad (2)$$

## 3. RESULTS AND DISCUSSION

*3.1 $Pd_2SnP_x$ nanorods*

Figure 1a displays a representative TEM micrograph of the particles obtained from the reaction of $Pd(acac)_2$ and $Sn(OAc)_2$ within OAm, MAC and TOP and the posterior phosphorization step at 300 °C using HMPT (see details in the experimental section). The produced nanoparticles displayed elongated morphologies with an average length and width of (24 ± 3) × (9 ± 1) nm (Figure 1a inset). This morphology resembled that of $Pd_2Sn$ nanorods produced following the same strategy but without the incorporation of HMPT.[25] The XRD pattern of the particles displayed an orthorhombic phase with space group Pnma, matching the reference pattern

from $Pd_2Sn$ (JCPDS 01-089-2057). No evidence of additional diffraction peak corresponding to secondary phases, such as tetragonal $Pd_5PSn$, $PdP_2$ or SnP, could be observed. HRTEM analysis (Figure 1c) results confirmed the orthorhombic (S.G.: Pnma) $Pd_2Sn$ phase with lattice parameters: a = 5.6500 Å, b = 4.3100 Å, c = 8.1200 Å. STEM-EELS elemental compositional maps unequivocally displayed the presence of Pd, Sn and P evenly distributed throughout the purified nanorods. EDS analysis confirmed the presence of P and allowed to quantify the overall elemental ratios as Pd/Sn/P = 2.1/1.0/2.2. To test the volatility of the measured phosphorous, samples were annealed under argon at 400 °C. After this process, EDS analysis showed a minor decrease of the phosphorus concentration: Pd/Sn/P = 2.1/1.0/1.7.

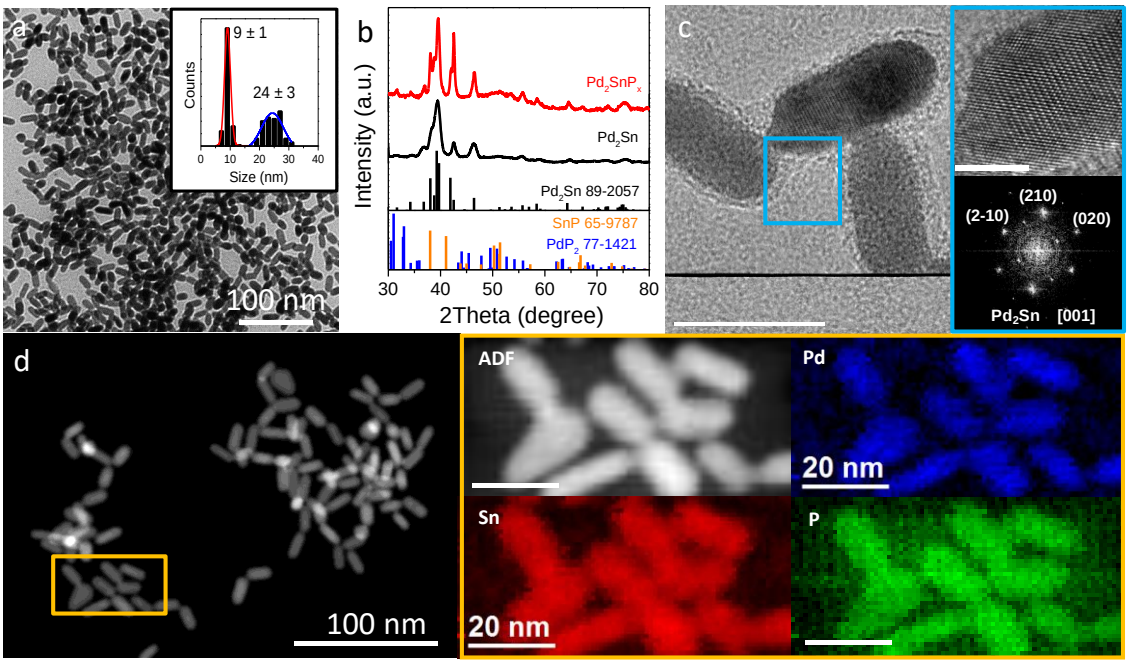


Figure 1. (a) TEM micrograph and histograms of the length (blue) and width (red) distribution of $Pd_2SnP_x$ nanorods. (b) XRD patterns of $Pd_2SnP_x$ and $Pd_2Sn$ nanorods. (c) HRTEM micrograph of $Pd_2SnP_x$ nanoparticles and power spectrum (FFT) of a particle visualized along its [001] zone axis. (d) HAADF-STEM micrograph of $Pd_2SnP_x$ particles and STEM – EELS elemental composition maps from the orange square area: Pd (blue), Sn (red) and P (green).

Figure 2 displays the XPS spectra of purified $Pd_2SnP_x$ nanorods and the $Pd_2SnP_x$/C catalyst. To prepare the catalysts, $Pd_2SnP_x$ particles were supported on carbon black and treated with acetic acid to displace organic ligands (see experimental section for details). The Pd 3d spectrum of the purified $Pd_2SnP_x$ nanorods exhibited one doublet at 335.4 ($3d_{5/2}$) and 340.6 eV ($3d_{3/2}$) that was assigned to a $Pd^0$ chemical environment (Figure 2a).[37,38] After preparing the catalyst, a second doublet appeared at 337.4 eV ($3d_{5/2}$) and 342.6 eV ($3d_{3/2}$) as shown in figure

2b. This doublet was ascribed to a $Pd^{2+}$ chemical state and accounted for ca. 14 % of the probed surface Pd.[37] The appearance of this oxidized component was associated with the exposure of the unprotected nanoparticles surface to ambient atmosphere during manipulation and transportation.

The Sn 3d spectra indicated the presence of two chemical states already in the purified $Pd_2SnP_x$ nanoparticles, before ligand displacement (Figure 2a). A first doublet at 484.6 eV (Sn $3d_{5/2}$) and 493.0 eV (Sn $3d_{3/2}$) was assigned to $Sn^0$ and accounted for 32 % of the probed Sn.[37,38] The second doublet, located at 486.6 eV (Sn $3d_{5/2}$) and 495.0 eV (Sn $3d_{3/2}$), was assigned to an oxidized Sn component, $Sn^{x+}$, and accounted for the other 68 % of the probed Sn.[37] After supporting the nanoparticles on carbon black and displacing the ligands, the oxidized Sn component increased up to the 77 % of the total Sn probed (Figure 2b).

Two phosphorous chemical states were also identified from the XPS analysis of the purified $Pd_2SnP_x$ nanoparticles, before ligand displacement (Figure 2a). These chemical states were assigned to P within a metal phosphide lattice, at 130.0 eV (P $2p_{3/2}$) and 130.9 (P $2p_{1/2}$), and an oxidized phosphorous form tentatively identified as a phosphate $(PO_4)^{3-}$, at 133.1 eV (P $2p_{3/2}$) and 134.0 (P $2p_{1/2}$).[16,37,39] The oxidized component accounted for ca. 65 % of the total P observed. When supported on carbon black and after ligand displacement, only the oxidized component was identified (Figure 2b).

The $Pd_2SnP_x$ surface atomic ratio, as determined by XPS, was Pd/Sn/P = 1/0.97/1.37. Therefore, taking into account EDS data, the surface of the $Pd_2SnP_x$ nanorods was Sn- and P-rich. This result correlated well with the higher percentages of oxidized tin and phosphorous obtained, and might be related to the higher tendency for these two elements to oxidize under ambient atmosphere compared with Pd. Similar results were obtained for $Pd_2Sn$, with an XPS elemental ratio of Pd/Sn = 1.2.[25]

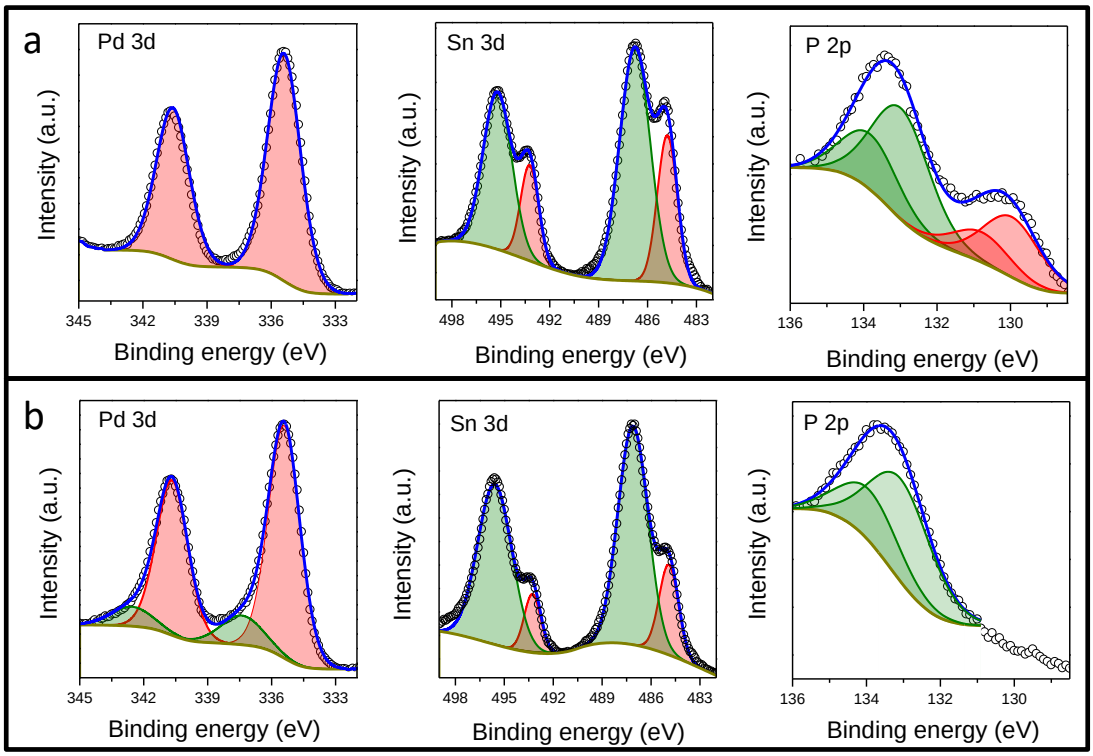


Figure 2. XPS spectra of Pd, Sn and P from $Pd_2SnP_x$ particles (a) and the $Pd_2SnP_x$/C catalyst (b).

*3.2 Electrocatalytic ethanol oxidation*

Figure 3a displays the CV curves recorded after 30 activation cycles. The current density peaks in the region between -0.5 V and -0.9 V vs. Hg/HgO were attributed to hydrogen adsorption in the cathodic scan and desorption in the anodic scan.[40,41] The current density peaks at ca. -0.2 V vs. Hg/HgO in the forward scan were associated with the oxidation of surface Pd. During the reverse scan, clear PdO reduction peaks were identified at around -0.2 V vs. Hg/HgO.

The electrochemical active surface area (ECSA) of the catalysts was estimated from the coulombic charge associated with the PdO reduction peak:

$$\mathrm{ECSA} = \frac{\mathrm{Q}\ (\mu C \cdot cm^{-2})}{Q_{PdO}(\mu C \cdot cm_{Pd}^{-2}) \times Pd_{loading}(mg \cdot cm^{-2}) \times 10}$$

where $Q_{PdO}$ = 405 µC $cm^{-2}$ was the charge associated to the reduction of a PdO monolayer, the coulombic charge Q was calculated by integrating the area of the PdO reduction peak, and the Pd loading was the amount of Pd on the working electrode.[12] Using this equation, ECSA values for Pd/C, $PdP_2$/C, $Pd_2Sn$/C and $Pd_2SnP_x$/C catalysts were 50.7 $m^2g^{-1}$, 61.1 $m^2g^{-1}$, 76.8 $m^2g^{-1}$, and 116.8 $m^2g^{-1}$, respectively. Notice that significantly larger ECSAs were obtained with the addition of Sn and P to Pd, and the highest ECSA was obtained when incorporating both elements simultaneously to obtain the $Pd_2SnP_x$/C catalyst.

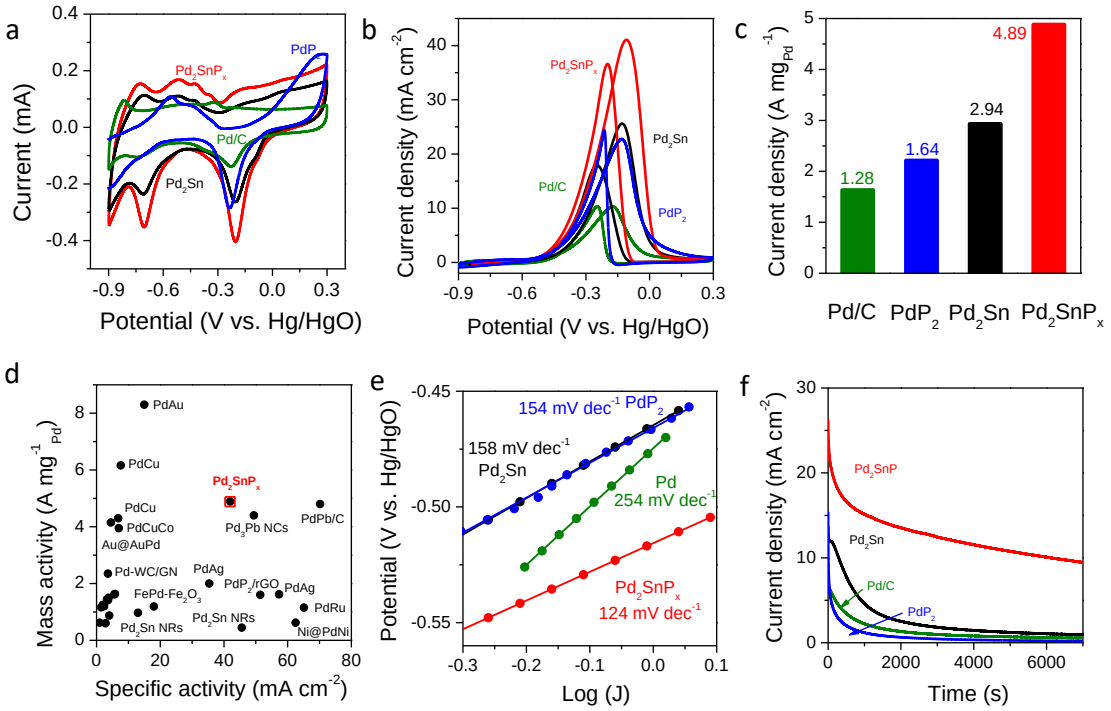


Figure 3. (a) CV curves (after 30 stabilization cycles) of $Pd_2SnP_x$/C, $Pd_2Sn$/C, $PdP_2$/C and commercial Pd/C catalysts in 0.5 M KOH aqueous solution. (b) CV curves, (c) mass peak current density and (d) Mass current density and specific current density of $Pd_2SnP_x$/C compared with Pd-based catalysts reported in the literature. (e) Tafel plots in 0.5 M KOH + 0.5 M EtOH aqueous solution. (f) CA data in 0.5 M KOH + 0.5 M EtOH aqueous solution at −0.1 V vs. Hg/HgO.

Figure 3b displays the CV curves of the electrocatalysts in 0.5 M KOH + 0.5 M EtOH solution. The two characteristic ethanol oxidation peaks were identified in the anodic and reverse scans for all the electrocatalysts tested. In the forward scan, the current density associated with the EOR started rising at ca. -0.55 V vs. Hg/HgO for all samples, and reached a maximum at a potential in the range from -0.10 V to -0.17 V vs. Hg/HgO, depending on the catalyst composition. Above these potentials, the current density decreased due to the surface oxidation of palladium. The catalyst containing phosphorous and/or tin displayed peaks at slightly higher potentials than the Pd/C catalyst. In the reverse scan, a sharp rise in the current density was triggered by the reduction of PdO at a voltage range between -0.08 V vs. Hg/HgO for $Pd_2SnP_x$/C and -0.18 for Pd/C. The presence of Sn and P promoted the EOR activity and best performance was obtained when both elements were alloyed together with Pd. $Pd_2SnP_x$/C catalyst was characterized by the highest peak current density up to 41.2 mA $cm^{-2}$, compared with the 25.5 mA $cm^{-2}$ for $Pd_2Sn$/C, 22.5 mA $cm^{-2}$ for $PdP_2$/C and 10.3 mA $cm^{-2}$ for Pd/C. These values resulted in dramatically high mass current densities, up to 4.89 A $mg_{Pd}^{-1}$ (Figure 3c), for

$Pd_2SnP_x$/C when compared with the reference catalysts tested here and those found in the literature. Figure 3d compares the specific and mass activities of $Pd_2SnP_x$/C with reported Pd-based catalysts further demonstrating that the simultaneous incorporation of Sn and P effectively improved the Pd activity toward EOR. [9,12,16,42-58] Additionally, the potential increase required to rise the current density was also significantly low for $Pd_2SnP_x$/C, especially when compared with commercial Pd/C, as noted in the Tafel plots displayed in figure 3e.

The electrocatalyst long-term stability was evaluated by chronoamperometry measurements (Figure 3f). All the catalysts showed a sharp current density decay during the first 1000 s, which was ascribed to the surface accumulation of strongly adsorbed intermediates that partially blocked the active sites. The $Pd_2SnP_x$/C catalyst showed a lower decay and was able to maintain much higher current densities during the whole chronoamperometric test, displaying very high current densities of 9.52 mA $cm^{-2}$ even after 7000 s operation.

*3.3 DFT Calculations*

To evaluate the effect of phosphorus, DFT calculations were carried out (computational details and models can be found on the experimental section and the supporting information). According to previous literature, in alkaline media, EtOH is dehydrogenated into adsorbed acetyl, which is further oxidized to acetate by hydroxide species. The oxidation of the acetyl to acetic acid by adsorbed hydroxyl is regarded as the rate-limiting step, while the stripping of the acetic acid in the form of acetate ions in alkaline solution is very rapid.[59,60] We calculated the $OH^-$ adsorption energies at different sites of the catalysts surface (Table 1) and related these values to the catalyst activity considering that a higher chemical adsorption of $OH^-$ increases activity by facilitating the formation of $CH_3COOH$.[61] For a pure $Pd_2Sn$ surface used as a reference, the average Bader charges for Pd and Sn species at the topmost layer are -0.282 and +0.596, respectively. As a result, the adsorption of $OH^-$ at Sn sites should be more energetically favorable than at Pd sites. Additionally, according to the optimized geometries, $OH^-$ tends to be located at the bridge or center but not at the top sites, i.e. Sn-Pd bridge, Pd-Pd bridge, and $Pd_3$ center. Due to the slightly different Bader charges, the adsorption energies for the bridge site of Sn-Pd dimers varies slightly with an average value of -0.821 eV. Furthermore, in consideration of the large difference in adsorption energies between Pd- and Sn-relevant sites and the opposite charges, the selective adsorption of $CH_3CO$ radicals near Pd site and that of $OH^-$ near Sn ones is to be expected, which benefits the catalytic reaction. These results are consistent with the improved catalytic performances of $Pd_2Sn$ with respect to Pd toward EOR.[38]

When phosphorus was introduced into the system, two representative models were considered (Figure S1b and 1c). A first model corresponded to the incorporation of P within the $Pd_2Sn$ lattice electronically influencing Pd and Sn surface reaction sites and incorporating new adsorption sites. A second model considered the presence of oxidized P on the catalyst surface according to XPS results. In the first model, the Bader charges of Pd near P increased slightly, while those of Sn remained nearly unchanged, which can be confirmed by the EDD diagram in Figure S2 of the SI. The adsorption energies of $OH^-$ at different sites all decreased to a certain extent, which facilitated overcoming the EOR rate-limiting step. The lowest adsorption energies corresponded to the adsorption of $OH^-$ on top of P. In a second model, we took into account XPS results that experimentally evidenced the presence of oxidized P species, $PO_x$, on the catalyst surface. As shown in Figure S1c and Figure S3, due to the surface oxidation, Sn ions close to P are oxidized to a much higher valence state, and an electron transfer is clearly observed (Figure S3c). These significant changes in electronic structures lead to a larger decrease of the adsorption energies for $OH^-$ (Table S1), which we believe favored boosting the catalytic activity of the material. We believe that the promotion of the OH- adsorption not only contributed to increase the EOR activity, but was also helpful to oxidize poisoning species, thus increasing the catalyst stability.

Table 1 Adsorption energies for $OH^-$ on different sites of $Pd_2Sn$ and $Pd_2SnP_x$ surfaces, considering two sites and chemical states of P, within the lattice as P and at the surface as $PO_x$.

| | Sn-Pd bridge | Pd-Pd bridge | $Pd_3$ center | P top |
|---|---|---|---|---|
| $Pd_2Sn$ | -0.821 | -0.501 | -0.499 | – |
| $Pd_2Sn$ incorporating P | -0.851 | -0.552 | -0.580 | -0.925 |
| $Pd_2Sn$ incorporating surface $PO_x$ | -1.041 | -0.560 | -0.658 | – |

## CONCLUSIONS

In summary, $Pd_2SnP_x$ nanorods were synthesized through phosphorization of $Pd_2Sn$ nanocrystals with a highly active reagent-HMPT in a one-pot two-steps colloidal reaction. $Pd_2SnP_x$/C catalysts exhibited significantly enhanced activity and durability toward EOR in alkaline media, when compared with $Pd_2Sn$/C, $PdP_2$/C and commercial Pd/C catalysts. The introduction of P additionally improved the durability of $Pd_2SnP$ catalyst and resulted in lower Tafel slopes that denoted a faster charge transfer kinetics or a larger density of active sites. DFT calculations showed that the incorporation of phosphorous either as lattice P or as a surface phosphate, allowed reducing the $OH^-$ adsorption energy both through an electronic effect and a direct bifunctional role, thus contributing to overcome the rate limiting step in EOR and reducing the rate of adsorption of poisoning species.

## REFERENCES


(1) Lamy, C.; Belgsir, E. M.; Leger, J.-M. Electrocatalytic Oxidation of Aliphatic Alcohols : Application to the Direct Alcohol Fuel Cell ( DAFC ). *J. Appl. Electrochem.* **2001**, *31*, 799–809.

(2) Lamy, C.; Lima, A.; LeRhun, V.; Delime, F.; Coutanceau, C.; Le, J. Recent Advances in the Development of Direct Alcohol Fuel Cells (DAFC). *J. Power Sources* **2002**, *105*, 283–296.

(3) Antolini, E.; Gonzalez, E. R. Alkaline Direct Alcohol Fuel Cells. *J. Power Sources* **2010**, *195* (11), 3431–3450. https://doi.org/10.1016/j.jpowsour.2009.11.145.

(4) Antolini, E. Catalysts for Direct Ethanol Fuel Cells. *J. Power Sources* **2007**, *170*, 1–12. https://doi.org/10.1016/j.jpowsour.2007.04.009.

(5) Akhairi, M. A. F.; Kamarudin, S. K. Catalysts in Direct Ethanol Fuel Cell (DEFC): An Overview. *Int. J. Hydrogen Energy* **2016**, *41* (7), 4214–4228. https://doi.org/10.1016/j.ijhydene.2015.12.145.

(6) Bianchini, C.; Shen, P. K. Palladium-Based Electrocatalysts for Alcohol Oxidation in Half Cells and in Direct Alcohol Fuel Cells. *Chem. Rev.* **2009**, *109*, 4183–4206.

(7) Iqbal, M.; Kaneti, Y. V.; Kim, J.; Yuliarto, B.; Kang, Y.-M.; Bando, Y.; Sugahara, Y.; Yamauch, Y. Chemical Design of Palladium-Based Nanoarchitectures for Catalytic Applications. *Small* **2019**, 1804378. https://doi.org/10.1002/smll.201804378.

(8) Moraes, L. P. R.; Matos, B. R.; Radtke, C.; Santiago, E. I.; Fonseca, F. C.; Amico, S. C.; Malfatti, C. F. Synthesis and Performance of Palladium-Based Electrocatalysts in Alkaline Direct Ethanol Fuel Cell. *Int. J. Hydrogen Energy* **2016**, *41*, 6457–6468. https://doi.org/10.1016/j.ijhydene.2016.02.150.

(9) Zhu, F.; Ma, G.; Bai, Z.; Hang, R.; Tang, B.; Zhang, Z.; Wang, X. High Activity of Carbon Nanotubes Supported Binary and Ternary Pd-Based Catalysts for Methanol, Ethanol and Formic Acid. *J. Power Sources* **2013**, *242*, 610–620. https://doi.org/10.1016/j.jpowsour.2013.05.145.

(10) da Silva, S. G.; Assumpção, M. H. M. T.; Silva, J. C. M.; De Souza, R. F. B.; Spinacé, E. V.; Neto, A. O.; Buzzo, G. S. PdSn/C Electrocatalysts with Different Atomic Ratios for Ethanol Electro-Oxidation in Alkaline Media. *Int. J. Electrochem. Sci.* **2014**, *9* (10), 5416–5424.

(11) Geraldes, A. N.; Furtunato Da Silva, D.; Martins Da Silva, J. C.; Antonio De Sá, O.; Spinacé, E. V.; Neto, A. O.; Coelho Dos Santos, M. Palladium and Palladium-Tin Supported on Multi Wall Carbon Nanotubes or Carbon for Alkaline Direct Ethanol Fuel Cell. *J. Power Sources* **2015**, *275*, 189–199. https://doi.org/10.1016/j.jpowsour.2014.11.024.

(12) Wang, C.; Wu, Y.; Wang, X.; Zou, L.; Zou, Z.; Yang, H. Low Temperature and Surfactant-Free Synthesis of Pd2Sn Intermetallic Nanoparticles for Ethanol Electro-Oxidation. *Electrochim. Acta* **2016**, *220*, 628–634. https://doi.org/10.1016/j.electacta.2016.10.094.

(13) Liu, J.; Luo, Z.; Li, J.; Yu, X.; Llorca, J.; Nasiou, D. Applied Catalysis B : Environmental Graphene-Supported Palladium Phosphide PdP 2 Nanocrystals for Ethanol Electrooxidation. *Appl. Catal. B Environ.* **2019**, *242* (September 2018), 258–266. https://doi.org/10.1016/j.apcatb.2018.09.105.

(14) Wang, F.; Xue, H.; Tian, Z.; Xing, W.; Feng, L. Fe2P as a Novel e Fficient Catalyst Promoter in Pd/C System for Formic Acid Electro-Oxidation in Fuel Cells Reaction. *J. Power Sources* **2018**, *375* (October 2017), 37–42. https://doi.org/10.1016/j.jpowsour.2017.11.055.

(15) Li, P.; Zeng, H. C. Bimetallic Ni-Fe Phosphide Nanocomposites with a Controlled Architecture and Composition Enabling. **2018**, 2231–2238. https://doi.org/10.1039/c7ta10665c.

(16) Liu, J.; Luo, Z.; Li, J.; Yu, X.; Llorca, J.; Nasiou, D. Graphene-Supported Palladium Phosphide PdP2 Nanocrystals for Ethanol Electrooxidation. *Appl. Catal. B Environ.* **2019**, *242*, 258–266. https://doi.org/10.1016/j.apcatb.2018.09.105.

(17) Kucernak, A. R. J.; Fahy, K. F.; Sundaram, V. N. N. Facile Synthesis of Palladium Phosphide Electrocatalysts and Their Activity for the Hydrogen Oxidation , Hydrogen Evolutions , Oxygen Reduction and Formic Acid Oxidation Reactions. **2016**, *262*, 48–56.

(18) Liu, J.; Meyns, M.; Zhang, T.; Arbiol, J.; Cabot, A.; Shavel, A. Triphenyl Phosphite as the Phosphorus Source for the Scalable and Cost-E Ff Ective Production of Transition Metal Phosphides. **2018**. https://doi.org/10.1021/acs.chemmater.8b00290.

(19) Qiu, B.; Cai, L.; Wang, Y.; Lin, Z.; Zuo, Y.; Wang, M. Fabrication of Nickel – Cobalt Bimetal Phosphide Nanocages for Enhanced Oxygen Evolution Catalysis. *Adv. Funct. Mater.* **2018**, *28*, 1706008. https://doi.org/10.1002/adfm.201706008.

(20) Ma, J.; Chen, Y.; Chen, L.; Wang, L. Ternary Pd – Ni – P Nanoparticle-Based Nonenzymatic Glucose Sensor with Greatly Enhanced Sensitivity Achieved through Active-Site Engineering. *Nano Res.* **2017**, *10* (8), 2712–2720. https://doi.org/10.1007/s12274-017-1474-x.

(21) Liang, H.; Xia, C.; Jiang, Q.; Gandi, A. N.; Schwingenschlögl, U. Low Temperature Synthesis of Ternary Metal Phosphides Using Plasma for Asymmetric Supercapacitors. *Nano Energy* **2017**, *35*, 331–340. https://doi.org/10.1016/j.nanoen.2017.04.007.

(22) Jiang, R.; Tran, D. T.; Mcclure, J. P.; Chu, D. A Class of (Pd-Ni-P) Electrocatalysts for the Ethanol Oxidation Reaction in Alkaline Media. *ACS Catal.* **2014**, *4*, 2577–2586. https://doi.org/10.1021/cs500462z.

(23) Chang, J.; Feng, L.; Liu, C.; Xing, W.; Hu, X. An Effective Pd-Ni2P/C Anode Catalyst for Direct Formic Acid Fuel Cells. *Angew.Chem. Int. Ed.* **2014**, *53*, 122–126. https://doi.org/10.1002/anie.201308620.

(24) Feng, L.; Xue, H. Advances in Transition-Metal Phosphide Applications in Electrochemical Energy Storage and Catalysis. **2017**, 20–34. https://doi.org/10.1002/celc.201600563.

(25) Luo, Z.; Lu, J.; Flox, C.; Nafria, R.; Genç, A.; Arbiol, J.; Llorca, J.; Ibáñez, M.; Morante, J. R.; Cabot, A. Pd2Sn [010] Nanorods as a Highly Active and Stable Ethanol Oxidation Catalyst. *J. Mater. Chem. A* **2016**, *4* (42), 16706–16713. https://doi.org/10.1039/c6ta06430b.

(26) Bu, L.; Zhang, N.; Guo, S.; Zhang, X.; Li, J.; Yao, J.; Wu, T.; Lu, G.; Ma, J. Y.; Su, D. Biaxially Strained PtPb/Pt Core/Shell Nanoplate Boosts Oxygen Reduction Catalysis. *Science (80-. ).* **2016**, *354* (6318), 1410.

(27) Kresse, G.; Hafner, J. Ab Initio Melecular Dynamics for Liquid Metals. *Phys. Rev. B* **1993**, *47*, 558–561.

(28) Kresse, G.; Hafner, J. Ab Initio Melecular-Dynamics Simulation of the Liquid-Metal — amorphous-Semiconductor Transition in Germanium. *Phsical Rev. B* **1994**, *49*, 14251–14269.

(29) Kresse, G.; Furthmu, J. Efficient Iterative Schemes for Ab Initio Total-Energy Calculations Using a Plane-Wave Basis Set. *Phys. Rev. B* **1996**, *54*, 11169–11186.

(30) Kresse, G.; Furthmiiller, J. Efficiency of Ab-Initio Total Energy Calculations for Metals and Semiconductors Using a Plane-Wave Basis Set. *Comput. Mater. Sci.* **1996**, *6*, 15–50.

(31) Perdew, J. .; Burke, K.; Ernzerhof, M. Generalized Gradient Approximation Made Simple. *Phys. Rev. Lett.* **1996**, *77*, 3865–3868.

(32) Projector Augmented-Wave Method. *Phys. Rev. B* **1994**, *50*, 17953–17979.

(33) Monkhorst, H. J.; Pack, J. D. Special Points for Brillouin-Zone Integrations. *Phys. Rev. B* **1976**, *13*, 5188–5192.

(34) Phys, J. C.; Grimme, S.; Antony, J.; Ehrlich, S.; Krieg, H. A Consistent and Accurate Ab Initio Parametrization of Density Functional Dispersion Correction ( DFT-D ) for the 94 Elements H-Pu. *J. Chem. Phys.* **2010**, *132*, 154104. https://doi.org/10.1063/1.3382344.

(35) Grimme, S.; Ehrlich, S.; Goerigk, L. Effect of the Damping Function in Dispersion Corrected Density Functional Theory. *J. Comput. Chem.* **2011**, *32*, 1456–1465. https://doi.org/10.1002/jcc.

(36) Luo, Y.; Li, X.; Cai, X.; Zou, X.; Kang, F.; Cheng, H.; Liu, B. Two-Dimensional MoS2 Confined Co(OH)2 Electrocatalysts for Hydrogen Evolution in Alkaline Electrolytes. *ACS Nano* **2018**, *12*, 4565–4573. https://doi.org/10.1021/acsnano.8b00942.

(37) Moulder, J. F.; Stickle, W. F.; Sobol, P. E.; Bomben, K. D. *Handbook of X-Ray Photoelectron Spectroscopy: A Reference Book of Standard Spectra for Identification and Interpretation of XPS Data*; PerkinElmer, Physical Electronics Division: Eden Prairie, MN, 1992.1992.

(38) Luo, Z.; Lu, J.; Flox, C.; Nafria, R.; Genç, A.; Morante, J. R.; Cabot, A. Pd2Sn[010]Nanorods as a Highly Active and Stable Ethanol Oxidation Catalyst. *J.Mater.Chem.A* **2016**, *4*, 16706–16713. https://doi.org/10.1039/c6ta06430b.

(39) Liu, J.; Wang, S.; Kravchyk, K.; Ibáñez, M.; Nasiou, D.; Me-, M.; Llorca, J.; Arbiol, J.; Kovalenko, M. V; Cabot, A. SnP Nanocrystals as Anode Material for Na-Ion Battery. *J.Mater.Chem.A* **2018**, *6*, 10958–10966.

(40) Capacitors, E. What Are Batteries , Fuel Cells , and Supercapacitors ? *Chem. Rev.* **2004**, *104*, 4245–4269. https://doi.org/10.1021/cr020730k.

(41) Liang, Z. X.; Zhao, T. S.; Xu, J. B.; Zhu, L. D. Electrochimica Acta Mechanism Study of the Ethanol Oxidation Reaction on Palladium in Alkaline Media. **2009**, *54*, 2203–2208. https://doi.org/10.1016/j.electacta.2008.10.034.

(42) Liu, J.; Zheng, Y.; Hong, Z.; Cai, K.; Zhao, F.; Han, H. Microbial Synthesis of Highly Dispersed PdAu Alloy for Enhanced Electrocatalysis. *Sci. Adv.* **2016**, e1600858.

(43) Liu, J.; Huang, Z.; Cai, K.; Zhang, H.; Lu, Z.; Li, T.; Zuo, Y.; Han, H. Clean Synthesis of an Economical 3D Nanochain Network of PdCu Alloy with Enhanced Electrocatalytic Performance towards Ethanol Oxidation. *Chem.Eur.J.* **2015**, *21*, 17779–17785. https://doi.org/10.1002/chem.201503432.

(44) Zhao, X.; Dai, L.; Qin, Q.; Pei, F.; Hu, C.; Zheng, N. Self-Supported 3D PdCu Alloy Nanosheets as a Bifunctional Catalyst for Electrochemical Reforming of Ethanol. *Small* **2017**, *13*, 1602970. https://doi.org/10.1002/smll.201602970.

(45) Bi, C.; Feng, C.; Miao, T.; Song, Y.; Wang, D.; Xia, H. Understanding the e Ff Ect of Ultrathin AuPd Alloy Shells of Irregularly Shaped Au@AuPd Nanoparticles with High-Index Facets on Enhanced. *Nanoscale* **2015**, *7*, 20105–20116. https://doi.org/10.1039/c5nr06035d.

(46) Shu, Y.; Shi, X.; Ji, Y.; Wen, Y.; Guo, X.; Ying, Y.; Wu, Y.; Yang, H. Hollow Echinus-like PdCuCo Alloy for Superior Efficient Catalysis of Ethanol. *ACS Appl.Mater.Interfaces* **2018**, *10*, 4743–4749. https://doi.org/10.1021/acsami.7b17731.

(47) Yu, X.; Luo, Z.; Zhang, T.; Tang, P.; Li, J.; Wang, X.; Llorca, J.; Arbiol, J.; Liu, J.; Cabot, A. Stability of Pd3Pb Nanocubes during Electrocatalytic Ethanol Oxidation. *Chem.Mater.* **2020**, *32*, 2044–2052. https://doi.org/10.1021/acs.chemmater.9b05094.

(48) Wu, P.; Huang, Y.; Zhou, L.; Wang, Y.; Bu, Y.; Yao, J. Nitrogen-Doped Graphene Supported Highly Dispersed Palladium-Lead Nanoparticles for Synergetic Enhancement of Ethanol Electrooxidation in Alkaline Medium. *Electrochim. Acta* **2015**, *152*, 68–74. https://doi.org/10.1016/j.electacta.2014.11.110.

(49) Yang, J.; Xie, Y.; Wang, R.; Jiang, B.; Tian, C.; Mu, G.; Yin, J.; Wang, B.; Fu, H. Synergistic Effect of Tungsten Carbide and Palladium on Graphene for Promoted Ethanol Electrooxidation. *ACS Appl.Interfaces* **2013**, *5*, 6571–6579. https://doi.org/10.1021/am401216s.

(50) Wang, Y.; He, Q.; Guo, J.; Wang, J.; Luo, Z.; Shen, T. D.; Ding, K.; Khasanov, A.; Wei, S.; Guo, Z. Ultra Fine FePd Nanoalloys Decorated Multiwalled Cabon Nanotubes toward Enhanced Ethanol Oxidation Reaction. *ACS Appl.Mater.Interfaces* **2015**, *7*, 23920–23931. https://doi.org/10.1021/acsami.5b06194.

(51) Fu, S.; Zhu, C.; Du, D.; Lin, Y. Facile One-Step Synthesis of Three-Dimensional Pd-Ag Bimetallic Alloy Networks and Their Electrocatalytic Activity toward Ethanol Oxidation. *ACS Appl.Mater.Interfaces* **2015**, *7*, 13842–13848. https://doi.org/10.1021/acsami.5b01963.

(52) Bin, D.; Yang, B.; Zhang, K.; Wang, C.; Wang, J.; Zhong, J. Design of PdAg Hollow Nanoflowers through Galvanic Replacement and Their Application for Ethanol Electrooxidation. *Chem.Eur.J.* **2016**, *22*, 16642–16647. https://doi.org/10.1002/chem.201601544.

(53) Zhang, K.; Bin, D.; Yang, B.; Wang, C.; Ren, F.; Du, Y. Ru-Assisted Synthesis of Pd/Ru Nanodendrites with High Activity for Ethanol Electrooxidation. *Nanoscale* **2015**, *7*, 12445–12451. https://doi.org/10.1039/c5nr02713f.

(54) Guo, F.; Li, Y.; Fan, B.; Liu, Y.; Lu, L.; Lei, Y. Carbon- and Binder-Free Core- Shell Nanowire Arrays for E Fficient Ethanol Electro-Oxidation in Alkaline Medium. *ACS Appl.Mater.Interfaces* **2018**, *10*, 4705–4714. https://doi.org/10.1021/acsami.7b16615.

(55) Xue, J.; Han, G.; Ye, W.; Sang, Y.; Li, H.; Guo, P.; Zhao, X. S. Structural Regulation of PdCu 2 Nanoparticles and Their Electrocatalytic Performance for Ethanol Oxidation. *ACS Appl.Mater.Interfaces* **2016**, *8*, 34497–34505. https://doi.org/10.1021/acsami.6b13368.

(56) Ye, S.; Feng, J.; Li, G. Pd Nanoparticle/CoP Nanosheet Hybrids: Highly Electroactive and Durable Catalysts for Ethanol Electrooxidation. *ACS Catal.* **2016**, *6*, 7962–7969. https://doi.org/10.1021/acscatal.6b02263.

(57) Miao, T.; Song, Y.; Bi, C.; Xia, H.; Wang, D.; Tao, X. Correlation of Surface Ag Content in AgPd Shells of Ultrasmall Core-Shell Au@ AgPd Nanoparticles with Enhanced Electrocatalytic Performance for Ethanol Oxidation. *J.Phys.Chem.C* **2015**, *119*, 18434–18443. https://doi.org/10.1021/acs.jpcc.5b05571.

(58) Zhang, G.; Wu, J.; Xu, B. Syntheses of Sub-30 Nm Au@ Pd Concave Nanocubes and Pt-on-(Au@Pd) Trimetallic Nanostructures as Highly E Ffi Cient Catalysts for Ethanol Oxidation. *J.Phys.Chem.C* **2012**, *116*, 20839–20847. https://doi.org/10.1021/jp304570c.

(59) Sarma, S. C.; Peter, S. C. Understanding Small-Molecule Electro-Oxidation on Palladium Based Compounds-a Feature on Experimental and Theoretical Approaches. *Dalt. Trans* **2018**, *47*, 7864–7869. https://doi.org/10.1039/c8dt00443a.

(60) Wu, Z.; Miao, B.; Hopkins, E.; Park, K.; Chen, Y.; Jiang, H.; Zhang, M.; Zhong, C.; Wang, L. Poisonous Species in Complete Ethanol Oxidation Reaction on Palladium Catalysts. *J. Phys. Chem. C* **2019**, *123*, 20853–20868. https://doi.org/10.1021/acs.jpcc.9b04229.

(61) Chen, L.; Lu, L.; Zhu, H.; Chen, Y.; Huang, Y.; Li, Y.; Wang, L. Improved Ethanol Electrooxidation Performance by Shortening Pd–Ni Active Site Distance in Pd-Ni-P Nanocatalysts. *Nat. Commun.* **2017**, *8*, 14136. https://doi.org/10.1038/ncomms14136.